PAPER • OPEN ACCESS

Data-driven prediction of the performance of enhanced surfaces from an extensive CFD-generated parametric search space

To cite this article: A Larrañaga *et al* 2023 *Mach. Learn.: Sci. Technol.* **4** 025012

View the article online for updates and enhancements.

MACHINE LEARNING
Science and Technology

PAPER

OPEN ACCESS

Data-driven prediction of the performance of enhanced surfaces from an extensive CFD-generated parametric search space

A Larrañaga[1], S L Brunton[2], J Martínez[1,3], S Chapela[1] and J Porteiro[1,*]

[1] CINTECX, University of Vigo, Lagoas-Marcosende s/n, 36310 Vigo, Pontevedra, Spain
[2] Department of Mechanical Engineering, University of Washington, Seattle 98195 WA, United States of America
[3] CITMAga, 15782 Santiago de Compostela, Spain
[*] Author to whom any correspondence should be addressed.

E-mail: porteiro@uvigo.gal

Abstract

Machine learning has rapidly been adopted in virtually all areas of engineering in recent years. This paper develops a machine learning model capable of predicting the performance of parametrically generated enhanced microsurface geometries for cooling electronic and power systems. Designing this type of geometry usually involves expensive computational fluid dynamics (CFD) simulations, limiting the number of candidate geometries that may be tested. For this reason, when searching for new geometries for a given application, designs are usually restricted to a simplified subset of basic shapes to reduce the complexity and dimension of the search space. In an effort to add geometrical diversity and explore singular morphologies, we have developed an algorithm capable of characterizing almost any geometry, based on an extensive CFD database with more than 15 800 geometries obtained from a Monte Carlo sampling of the space of possible geometries. With this framework, it is possible to estimate various quantities of interest, such as the heat flux in the enhanced zone and total drag, with relative errors below 10% and 2%, respectively. Thus, we establish the utility of machine learning to develop surrogate models for the rapid performance prediction of novel enhanced microsurfaces.

1. Introduction

Many industrial processes require more efficient heat dissipation and transfer mechanisms. These processes include large-scale power generation plants [1], battery thermal management systems [2], and ubiquitous computer and telecommunications technologies [3]. Enhanced surface design is a branch of engineering with great importance that can be applied in the development of efficient heat dissipation or storage equipment across these scales of size and cost [4]. Currently, there is a need to rethink the designs of conventional heat exchangers toward new, more compact geometries that can benefit from advances in the additive manufacturing sector [5]. Similarly, the use of lasers is enabling the creation of highly challenging geometries with increasing degrees of freedom, resulting in the development of entirely new geometries [6, 7]. Beyond modifying the geometry, it is also possible to enhance thermal properties by the use of coating materials or treatments [8]. In nature, there are abundant examples of exotic fin and appendage morphologies that serve various purposes, such as cooling, producing lift or thrust, steering, and even ornamentation [9–11]. However, engineering surface design is often limited to simplified search spaces due to the computational expense of iterative design optimization based on computational fluid dynamics (CFD). Such approach has been extensively used in the past for multiobjective airfoil design [12], single-objective heat exchanger design [13], optimization of vortex generators [14], among others.

The focus of this work is to leverage emerging techniques in machine learning to develop computationally efficient surrogate models that may be used to broaden the design space of possible geometries [15–17].

Previous studies have focused on the optimization of enhanced surfaces by the modification of one or more design features already known to be relevant for the optimization of a particular quantity. From an

experimental perspective, See *et al* [18] performed a topological optimization for natural convection by minimizing the global thermal compliance in the solution of the modified momentum equation. Moze *et al* [19] aimed to develop the optimal surface pattern on low- and high-wetting regions for enhanced boiling heat transfer in aluminum superbiphilic surfaces. Related studies have focused on the wettability gradient for optimization purposes [20]. At the microscale, some work has been done on the optimization of microscale porous surfaces, using an experimental approach [21]. Furthermore, more traditional concepts have been adopted and widely investigated from a numerical perspective for the optimization of heat exchanger design through multiobjective genetic algorithms [13, 22], applying volume averaging theory [23], or directly using CFD evaluations for thermal evaluations [24]. More broadly, interest in heat transfer enhancement mechanisms has increased in recent years with the hope of developing new designs that could maintain their performance while minimizing overall production costs [25, 26]. Such interest has been benefited from the development of techniques related to neural networks applied to both fluid mechanics and heat transfer modeling [27, 28].

Machine learning can aid the development of technological advances of many sectors, including engineering [29]. It has actively been used for the development of digital twins based on physics-based models [30], applied both for experimental research [31] and industrial facilities [32]. More specifically, in the area of fluid mechanics there are several applications related to closure of Reynolds-averaged Navier–Stokes models against Direct Numerical Simulation [33], turbulence modeling [34] and flow control [35], enhancement of CFD [36], or surrogate modeling of complex systems to avoid extensive computational simulation times [37] with proven success.

In this article we seek to approach fin optimization from a data-driven perspective, leveraging machine learning to characterize and explore a richer geometric design space than would be traditionally possible with CFD alone. These novel data-driven tools are already being investigated in a range of fluid mechanics applications [38]. Here, we develop and train an algorithm to predict the performance of any possible fin that belongs to a range of the possible geometries that satisfy feasibility constraints. Once the algorithm is trained, it can be used as a surrogate model to predict the performance of new fin geometries in a larger multitarget optimization routine. In this way, starting from a planar geometry with 15 degrees of freedom, random combinations of different input values are used to generate an extensive offline CFD database. This database is then used to train different machine learning algorithms to predict the performance of the enhanced surfaces without the further need to run costly numerical simulations.

Section 2 of this article explains the parameterization of the selected geometries following Monte Carlo approximation. This is continued by the explanation of the generalization to adapt the numerical simulation to the space of possible cases studied. Finally, the different algorithm architectures tested are presented in more detail in section 3 and the training and evaluation criteria are included in section 4 to justify the results obtained on the most efficient geometries (presented in section 5). We believe that with the proven success of this novel approach, it can be applied to many other study cases as well.

2. Data generation

This section describes how the database of 15 860 numerical simulations is generated. We start with the explanation of the methodology used to sample geometries (section 2.1), followed by a description of the numerical scheme used in the CFD simulation (section 2.2). This is then followed by the thermal and fluid dynamic definition of the ribbed surface performance (section 2.3).

2.1. Geometry parametrization

As a first example, a concrete case was considered in which a hot surface is to be cooled. The setting is similar to surface cooling of a planar battery pack in which the separation of the channels is 2.5 mm and the other two dimensions (length and depth) are much higher. The bottom of the surface is set at 350 K and a flow of water at atmospheric pressure and 303 K enters the domain with a bulk velocity of 1 m s^{-1}. In the direction of the flow, the domain is varied in length to contain the established number of fins. The results of each case will be postprocessed to account for the difference in lengths among the cases.

A total of 15 fins were placed longitudinally, where the domain length was adapted to the dimensions of the particular fin (shown at the top of figure 1). The highlighted intermediate zone, which goes from the seventh to the ninth fin, is used as the area of interest for the heat transfer study, as this region is less affected by the inflow turbulence and the multiple vortices that can be formed at the outlet.

Figure 1 shows a diagram of the parameterization of the geometry, where eight vertices and the intermediate separation between fins have been selected as the parameters of interest. Considering a local
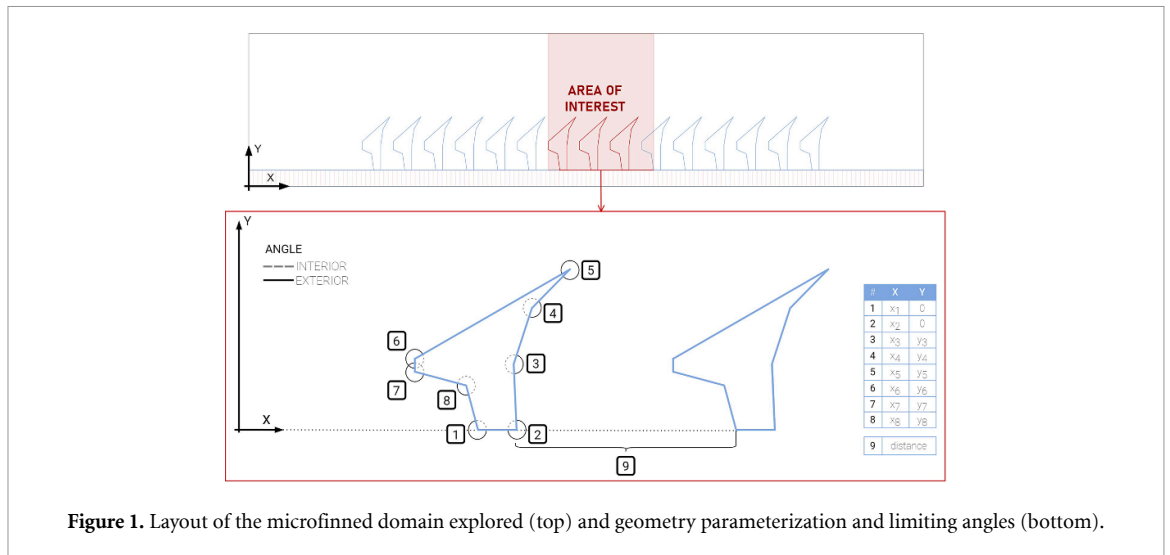
Figure 1. Layout of the microfinned domain explored (top) and geometry parameterization and limiting angles (bottom).
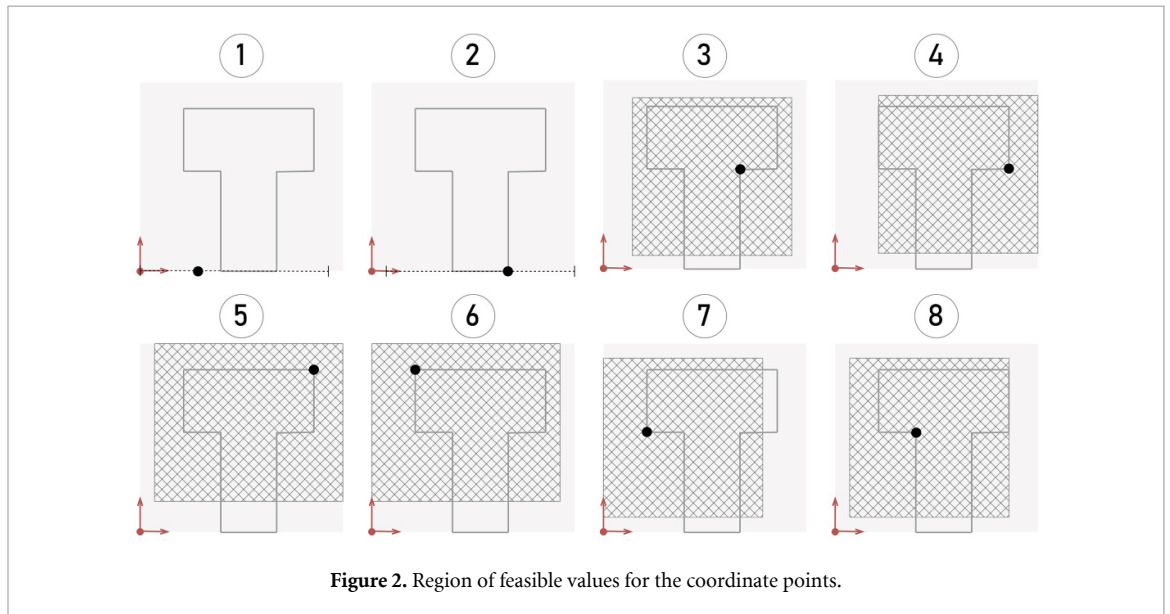

Figure 2. Region of feasible values for the coordinate points.

coordinate system to the fin, whose origin is shown as the red location in figure 2, the vertices can vary from 0 to 396 μm in the *x*-axis direction and up to 455 μm in the *y*-axis. The distance between fins, identified as 9 in figure 1, can range from 244 μm to 976 μm. Finally, both interior and exterior angles are monitored to avoid geometries that could be exposed to high mechanical stresses. Hence, angles below 15° are discarded, as this angle is identified as the minimum angle to maintain the numerical solution stability.

Figure 2 represents the space of possible solutions (striped area) for each of the coordinates that define the geometry. That is, each location (defined by the nomenclature according to figure 1) can take a value within the marked area, having two exceptions in the case of x_1 and x_2 that can only vary in the horizontal direction and not vertically.

The goal of this large space of possible solutions is to consider geometries that would be hard to imagine and design traditionally. However, this point of view brings in several challenges. First, the enormous number of cases to be simulated to cover the entire space of potential solutions, and second, the possible combination of points that could create infeasible geometries.

The number of simulations that would be required to cover the entire solution space increases exponentially with the number of splits in each parameter. This number of splits refers to the variability allowed within the same input feature. That is, if only the minimum and maximum are used this would count as two splits for each parameter, and so on. Therefore, even for a small number of splits, this quickly

Figure 3. Pipeline of the geometry generation algorithm.
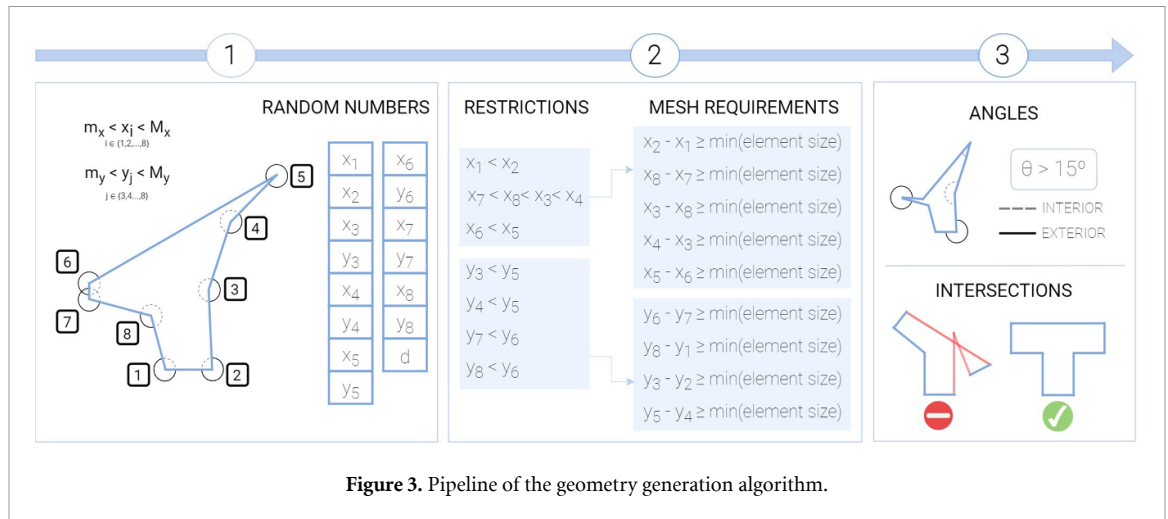
Table 1. Initial and boundary conditions (left) and materials (right).

Boundary conditions			Materials		
Mass flow inlet	2.5	(kg s^{-1})	*Fluid: water*		
$P_{outlet,g}$	0	(Pa)	Density	998.2	(kg m^{-3})
T_{inlet}	303	(K)	Specific heat	4182	(J (kg K)$^{-1}$)
T_{outlet}	303	(K)	Thermal conductivity	0.6	(W (m K)$^{-1}$)
T_{bottom}	350	(K)	Dynamic viscosity	0.001003	(kg (m s)$^{-1}$)
Turb. intensity at inlet	5	(%)	*Solid: aluminum*		
Turb. viscosity ratio at inlet	10	(—)	Density	2719	(kg m^{-3})
			Specific heat	871	(J (kg K)$^{-1}$)
			Thermal conductivity	202.4	(W (m K)$^{-1}$)

becomes computationally intractable. Accordingly, a more conservative approach was chosen, leveraging Monte Carlo sampling to obtain variability in the resulting geometries.

Specifically, figure 3 shows the pipeline that was applied. We started with the definition of the maximum and minimum values for each of the coordinates. We then generated a series of random numbers that remain between the boundaries of the 15 parameters. Then, a series of restrictions were applied, which can also be seen in figure 3, to ensure two properties were respected: (1) no line crossings and (2) the minimum distance between two contiguous points was higher than the minimum element size selected for the mesh. As a final constraint, it was verified that the resulting geometry did not contain angles sharper than 15°.

By processing millions of candidate geometries, a total of 15 860 valid geometries were generated, whose geometrical descriptions and CFD simulation results were used for the subsequent training of our machine learning (ML) algorithm.

2.2. Numerical generalization

To simulate the cases, geometry parameterization was used to automatically run a batch of cases simultaneously with ANSYS, a commercial software. The dimensions of the domain were adapted to the design of the microfins, as well as the spacing between them, keeping a constant channel height of 2.5 mm. In this way, a 5 mm inlet section and a 7.5 mm outlet segment were permanently maintained to avoid backflow and allow flow stabilization.

Table 1 contains the general boundary and initial conditions, as well as the materials utilized for both the fluid and the solid section. The no-slip condition was adopted for the walls. It is important to note that to apply the heat source, a 0.1 mm thick surface was added in the area below the fins (referred to as 'bottom' in table 1) in order to apply the heat source uniformly and to facilitate postprocessing.

The k-omega shear stress transport (SST) turbulence model was utilized with low-Re corrections, since the Reynolds number of the channel is approximately 2000. Due to the nature of the problem, there are two different timescales involved: a macroscopic time scale for the stabilization of the temperature map on the solid wall, the fins and the flow, and a much smaller microscopic time scale for the vortex and different flow structures inside the domain. Hence, the SIMPLE pressure–velocity coupling scheme was employed, and the

solution of the case was split into two time sections: an initial 100 s window was solved to allow the heat to flow and stabilize through the domain. 100 s proved to be sufficient to spread the heat over the domain and reach the quasi-steady solution of the flow. This was followed by 1000 smaller time steps to capture the transient nature of the structures formed by the presence of fins. To work with a Courant number close to unity, a time step size of 10×10^{-5} s was adopted for this second transient window.

Automatically setting the mesh size for the wide range of domains was probably the most time-consuming step since it had to be adapted to the diversity of geometries generated by this study, which, given the nature of the dataset, is not *a priori* known. To circumvent this limitation, a specific study was first made for the 'limit cases', which are those that have all their parameters fixed at an extreme value (lower or upper). These limit cases represent the boundary of our dataset and are therefore believed to be a good representation of the variety of subsequent geometries that will require being meshed.

Once the mesh methodology was established and validated for the 'limit cases', it was kept the same for the whole dataset. In this methodology, the domain is first divided into three zones in which the mesh goes from the finest, in the region around the fins, to the coarsest in the region near the center of the channel. The first zone finishes at a vertical coordinate of 0.75 mm, and the second zone finishes at 1.25 mm. The number of elements in the mesh depended greatly on the geometry but generally ranged from 0.5 to 1 M cells. In addition, the skewness remained between 0.1 and 0.2, with no appreciable deformed cells in the majority of the cases.

2.3. Fin performance evaluation

Thermal performance is mainly evaluated by means of heat flux (i.e. $\dot{Q}_{\mathrm{FINS}}$ (kWm^{-2})), average temperature (i.e. $\bar{T}$ (K)) and minimum temperature (i.e. T_{MIN} (K)). The last two are scaled with respect to a reference temperature (i.e. T_{REF} (K)), which is equivalent to the hot source temperature, 350 K. The evaluation of these variables was made considering only the intermediate section of the fin row. That is, the three central fins (corresponding to positions 7, 8, and 9) were selected to calculate the surface integral of the heat flux and temperature on the fins surface. It is important to note that the maximum temperature was not taken into account as a potential output because in general, it tended to remain very close to the temperature of the hot source, which hence lacks the required variability for the model to learn. Generally, in the space between the fins and due to the high conductivity of the aluminum, the temperature is close to 350 K, which was imposed on the surface.

On the other hand, the pressure drop is evaluated in the entire domain. Not only was the pressure differential between inlet and outlet considered but also the nondimensional drag coefficients (more specifically, total drag (i.e. C_{D}), pressure drag (i.e. C_{P}) and drag due to friction (i.e. C_{F}) were evaluated). These parameters embody the frictional forces (caused by wall shear stresses due to the fluid's viscosity) and pressure forces (caused by normal stresses as a result of different static pressure forces) that act on the microfin when the fluid flows around it. The sum of both coefficients determines the overall drag that is macroscopically experienced on the body.

Drag coefficients were calculated according to equation (2.1), considering the subscript x as the substitute for the chosen force in each case:

$$C_x = \frac{F_x}{\frac{1}{2}\rho v_\infty^2 A_s} \tag{2.1}$$

where ρ stands for the density of water, 998.2 kg m^{-3}, v_∞ is the bulk flow velocity, 1 m s^{-1}, and A_s is the surface area, 0.0025 m^2.

Fin efficiency, i.e. η, is defined as the ratio of heat flux through the finned area, i.e. $\dot{q}_{\mathrm{FINS}}$(kW), to what would be obtained with a fin at a constant temperature equal to the plain surface temperature (equation (2.2))

$$\eta = \frac{\dot{q}_{\mathrm{FINS}}}{h_{\mathrm{p}} A_{\mathrm{F}} \left(T_{\mathrm{wb}} - T_\infty\right)} \tag{2.2}$$

where h_{P} (kWm^{-2}K^{-1}) stands for the convective heat transfer coefficient for the plain surface case, A_{F}(m^2) stands for the ribbed surface area and T_{wb} (K) and T_∞ (K) represent the plain surface case wall temperature and bulk fluid temperature, respectively.

3. Mathematical background

Figure 4 shows the methodology used to train different machine learning algorithms to predict the various quantities of interest from a specification of the geometry. In particular, we will compare algorithms with
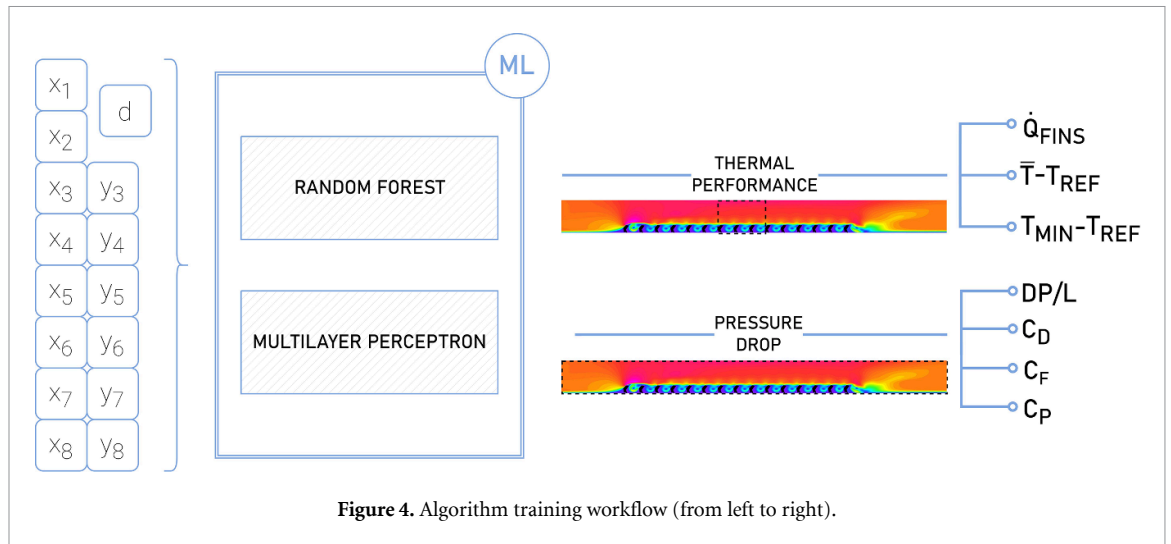
Figure 4. Algorithm training workflow (from left to right).

different architectures to assess how this model structure impacts our multidimensional predictions. The main challenge with this problem is the high dimensionality of the input space as a consequence of the parameterization. Therefore, we compare (1) random forest and (2) a multilayer perceptron (MLP) models, using vertex coordinates as input parameters.

Random forest is an ensemble learning method belonging to the class of supervised learning algorithms [39, 40]. This model is based on an ensemble of decision trees [41]. Each tree starts from one point and grows until the solution on the desired variable is reached. By using the ensemble approach, the prediction is further improved by averaging the predictions of all the trees that constitute the model.

On the other hand, an MLP [42], consists of a neural network comprised of a group of linear threshold units, which are structures that consist of one input x with n values, a single-value output, and intermediate mathematical calculations that form a linear combination of such inputs with their corresponding weights. This linear combination is then multiplied by an activation function that encourages the learning of the linear threshold unit. If more layers are included as hidden layers, then this architecture will be known as a deep neural network [42].

In addition to having a high-dimensional space as model input, there is also a multidimensional output comprised of the most relevant physical variables for studying the behavior of the ribbed surface from a thermal and fluid dynamic point of view.

4. Training and evaluation

Considering the amount of data available, to complete the training of the present algorithms, it was decided to follow a cross-validation approach [43]. Accordingly, the dataset was divided into 90% (training set) and 10% (test set), of which the former was used to perform a cross-validation with ten subgroups. In this way, a performance metric is obtained for the training and validation sets, keeping the initial 10% to perform a final test with the optimal model after hyperparameter optimization. Figure 5 shows a schematic of such a process, where s stands for the selected evaluation score (which in this case corresponds to mean absolute percentage error (MAPE) (equation (4.1)).

4.1. Metrics
To evaluate the trained models, the following metrics were used:

4.1.1. MAPE
Given $\hat{y}_i$ as the predicted value for the ith sample and y_i as the corresponding true value, MAPE can be estimated by the following equation over n_s:

$$\text{MAPE}(y, \hat{y}) = \frac{1}{n_s} \sum_{i=1}^{n_s} \frac{|y_i, \hat{y}_i|}{\max(\varepsilon, |y_i|)} \tag{4.1}$$

Figure 5. Training and evaluation workflow for each ML algorithm.
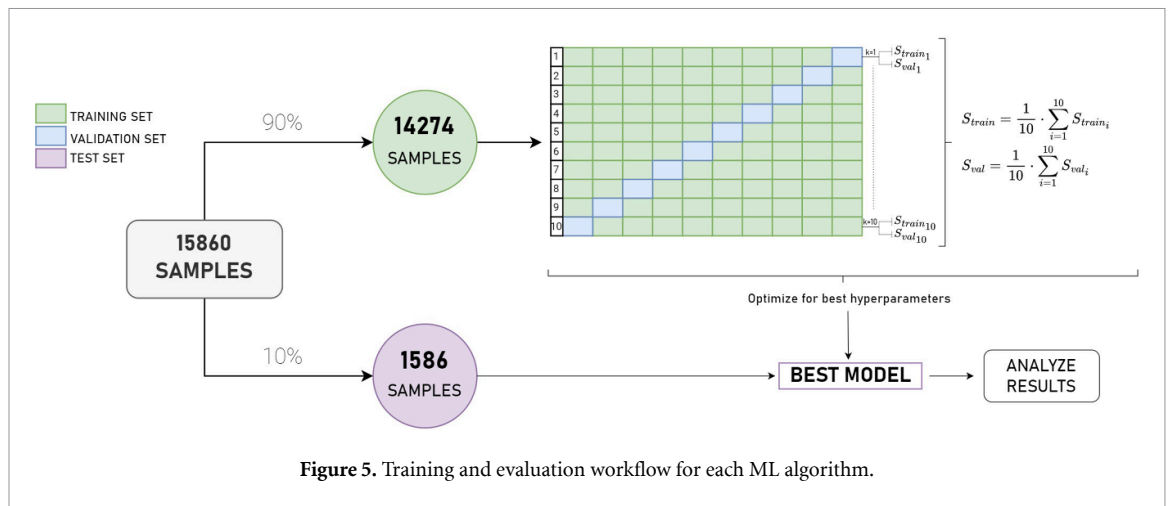
Table 2. Hyperparameters for the random forest regressor.

Random forest regressor		
Hyperparameters		**Range**
1	N° of decision trees that will be run by the ensemble method.	[20, 70, 100, 200, 500, 600, 700]
2	Max. depth of each individual tree.	[5, 15, 40, 55, 62, 70]
3	Max. n° of features considered when evaluating a split.	[4, 5, 6, 7]
4	Minimum n° of samples needed to split a node.	[5, 7, 9, 10, 20, 30]
5	Minimum n° of samples required to be a leaf node.	[1, 2, 3, 10, 20, 30]
6	Perform bootstrap	True

where n_s stands for the number of samples and ϵ is an arbitrary small positive number that avoids undefined solutions.

This metric has been chosen because of its sensitivity to relative errors.

4.1.2. Mean squared error (MSE)
Given $\hat{y}_i$ as the predicted value for the ith sample and y_i as the corresponding true value, MSE can be estimated by the following equation over n_s (which stands for number of samples):

$$\text{MSE}(y, \hat{y}) = \frac{1}{n_s} \sum_{i=1}^{n_s} (y_i - \hat{y}_i)^2. \tag{4.2}$$

This metric is commonly used for regression problems, corresponding to the expected value of the quadratic error.

4.2. Hyperparameter tuning
In the search for the optimal model to approximate the various physical variables mentioned in the previous section, each algorithm has a number of hyperparameters that can be altered to improve the fit. As the '*No Free Lunch*' theorem states, '*all optimization algorithms perform equally well when their performance is averaged across all possible problems*', which means that there is no combination of parameters that will adapt to every problem. Thus, it is an iterative process.

4.2.1. Random forest regressor
In the case of random forest, the choice of hyperparameters is closely related to the architecture of the trees that form the forest. Table 2 shows the different combinations of such parameters and their respective definitions.

4.2.2. MLP
For MLP tuning, four main hyperparameters were investigated, which are shown in table 3 with their respective names and descriptions.

Table 3. Hyperparameters for multilayer perceptron.

Multilayer perceptron		
Hyperparameters		
Name	*Description*	Range
1 Batch size	N° of training examples utilized in one iteration.	[32, 64, 128]
2 Activation function	Function that allows the learning of neurons by adding nonlinear variations.	relu
3 Optimizer	Functions that modifies the attributes of the architecture in order to reduce the overall loss and increase the accuracy.	[Adam, SGD, RMSPROP]
4 Neurons	N° of neurons of the hidden layer.	[50, 100, 200, 300]

5. Results

This section analyzes the results obtained from the single-phase flow, as well as the capacity of the different machine learning algorithms to model and predict the behavior of the physical variables of interest. Such analysis will follow what is known as '*surface performance comparison*' [44], since the effect of the hot source in the heat transfer process is not accounted for, the focus instead will be on a performance comparison with a smooth surface (i.e. the plain surface case).

It is important to note that the coordinates were allowed to vary within the limits set in section 2.1. Interestingly, and as will be seen in the next sections, most of the cases that reached their solution satisfactorily ended up situated in a nearby region.

5.1. Database diversity
The results here show the potential and variety in the geometries contained in the database. Although the main objective of this paper is not the development of an optimizer but rather a predictor that can be used later for optimization, it is interesting to analyze the type of geometries resulting from a descriptive analysis of the dataset studied.

Since this problem could be considered to be a multiobjective case, there is no single optimal solution. Depending on the user interest, the weight of the various outputs might be different (or even conflicting) leading to a complete range of solutions that meet the preferred choices. For the present problem, and as a visualization tool, a Pareto front was built by considering the combination of efficiency, pressure drop, single fin's perimeter and weight as the main variables of interest. However, these are just some of the possible variables that might be combined. Figure 6 shows the intersection between the selected variables, showing a dense cloud where the majority of the cases are located, together with some that show an outstanding performance that situates them closer (or forming) the Pareto frontier (black line).

In the first approach, thermal efficiency should be maximized, while the pressure drop should be kept minimal. If possible, the perimeter and weight should always be kept minimal since they represent potential costs.

As expected, the geometries that favor efficiency have in common a wide base that favors heat dissipation, and their separation allows the flow to reattach between fins. Their shape is quite simple without protuberances or beam structures that will increase the surface exposed to the cold flow but that will have low efficiency due to heat transfer limitations through the fin.

If perimeter is used as a limiting factor (let us say that an expensive coating is required), then the morphology of the fins changes slightly (shown in figure A1). On the other hand, those that minimize both weight and perimeter (figure A2) are not particularly careful to avoid narrow spaces and sharp corners. The configurations that tend to show the lowest pressure drop coincide with those that are flat, where the flow passes directly over the structure, as if the fin array were a bluff body, without truly having a chance to interact with the peculiarities of the design.

5.2. Thermal performance
Figure 7 shows a summary of the results obtained from the different geometries included in the database. Heat flux on the intermediate fins, i.e. $\dot{Q}_{\text{FINS}}$ (kWm^{-2}) follows a normal distribution with limiting cases close to zero, which is interesting because they are geometries that favor heat conservation rather than heat dissipation. In this case, they have not been considered negligible outliers but as geometries designed for a different purpose.
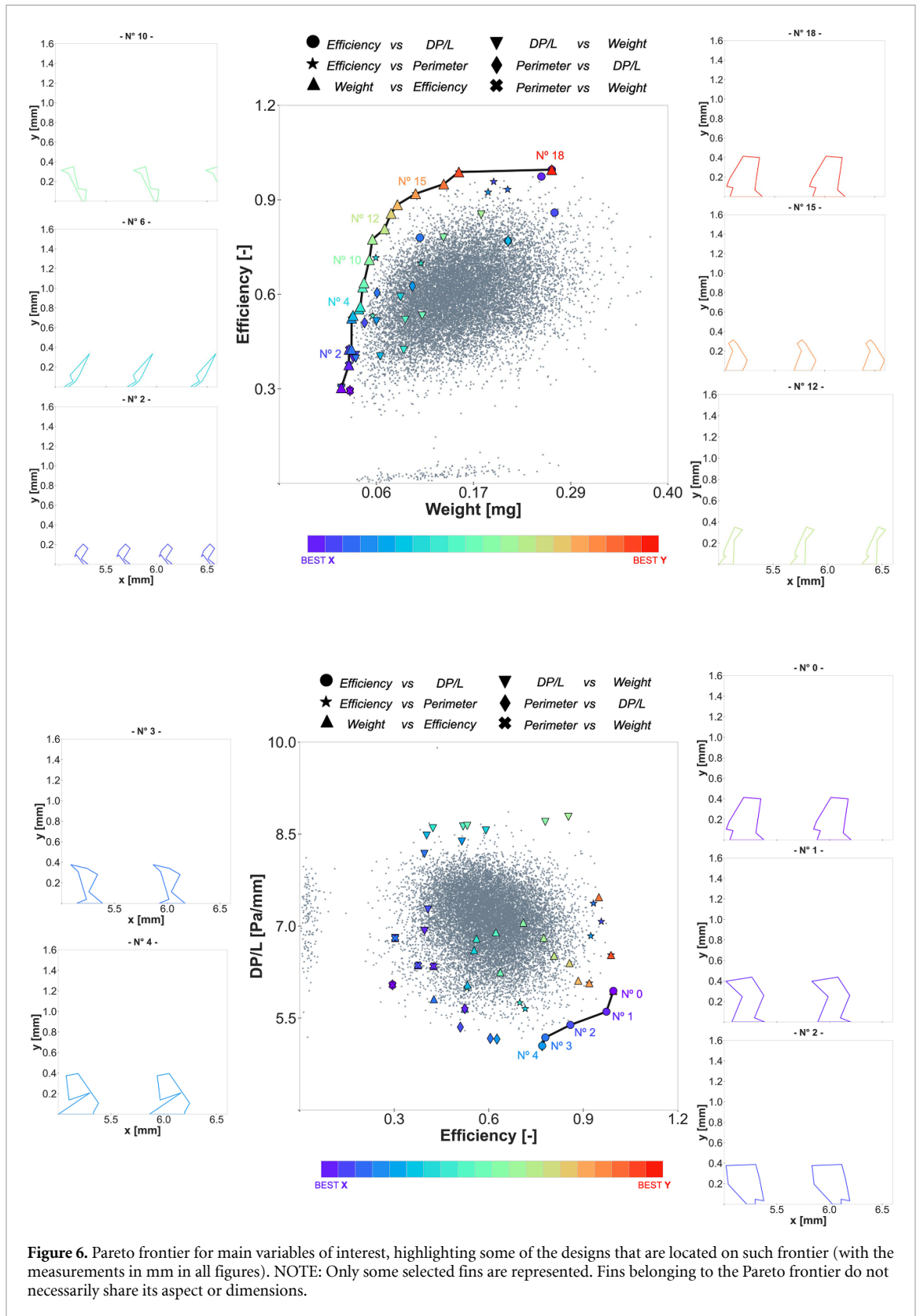
Figure 6. Pareto frontier for main variables of interest, highlighting some of the designs that are located on such frontier (with the measurements in mm in all figures). NOTE: Only some selected fins are represented. Fins belonging to the Pareto frontier do not necessarily share its aspect or dimensions.

The highest density of cases is concentrated within 800–1100 kW m^{-2}, which is nearly double the heat flux experienced in the plain surface case (roughly 520 kW m^{-2}, highlighted on the right-hand side heatmap). Moreover, most of the geometries' average temperature lie 5 K below the hot source set point, shown as the prominent peak in the temperature distribution figure.

Figure 7. On the left, histograms of $\dot{Q}_{\text{FINS}}$ *(top)*, $\bar{T}$ and T_{MIN} (bottom). On the right, a heatmap reflecting the intersection between $\dot{Q}_{\text{FINS}}$ and T_{MIN} regarding the thermal performance of the overall geometries. Moreover, the plain surface (i.e. baseline) case is plotted for reference in the heatmap.
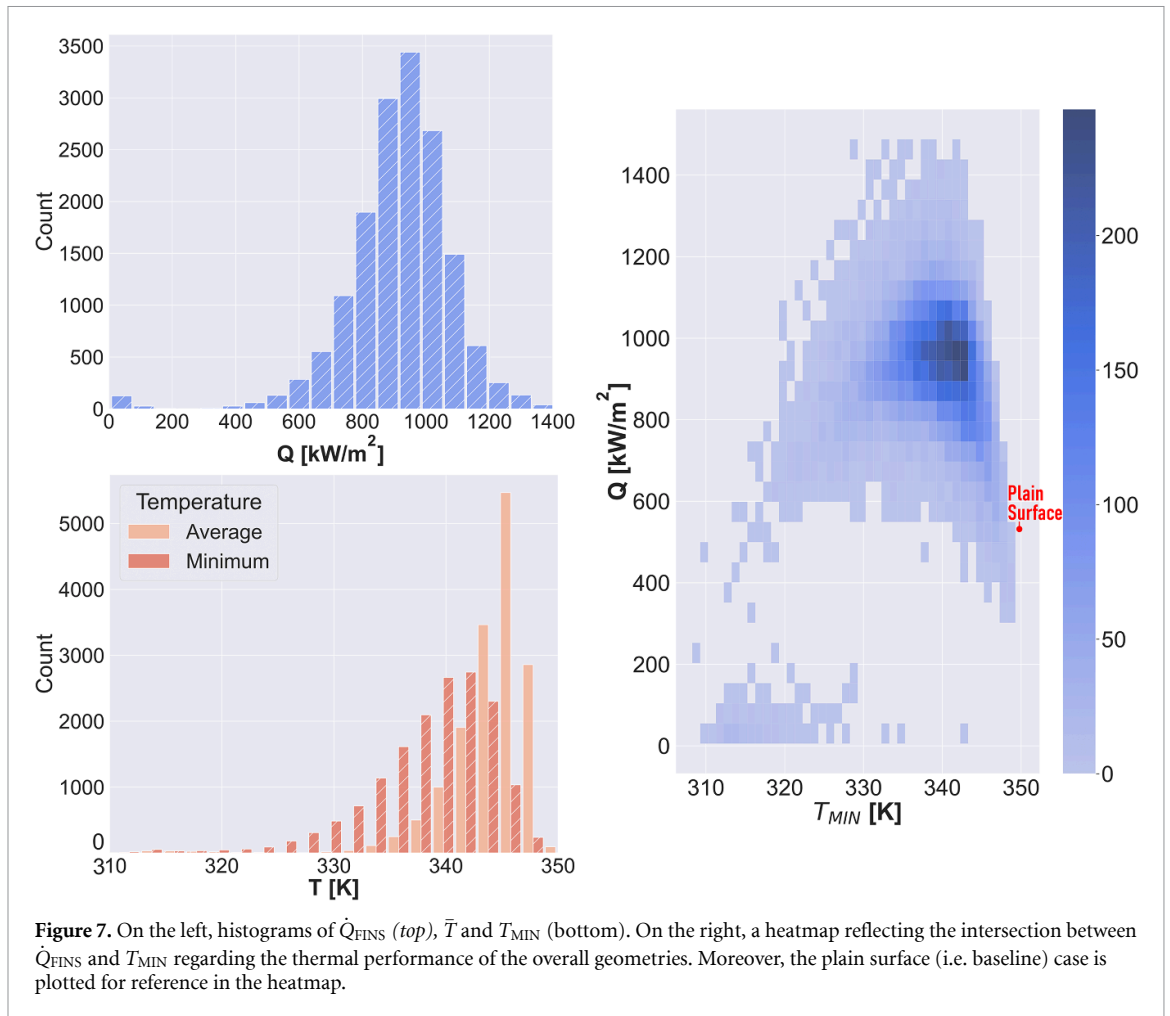
For the case of the minimum temperature, it is of particular interest because it is one of the most limiting factors and performance indicators when trying to maximize heat transfer over a surface. On the one hand, if the minimum temperature reached at the wall is close to the temperature of the hot source, it can be an indicator of a good heat exchange between sides that allows the material to work close to its physical limit (since it would never exceed the thermal conditions of its heat source). On the other hand, this same situation may be indicative of the exact opposite behavior; that is, if the fins are closely spaced and the geometry does not promote the formation of vortices in their separation, the fin array acts as a heat shield or a flow 'deflector' that impedes heat transfer. This is the case for fins that have a lower heat transfer performance than the plain surface case. These fins could be interesting for some applications but will not be the focus of the present work. It is interesting, however, that in terms of heat performance, there is a clear separation between those fins enhancing heat transfer (the majority) and those reducing it.

Figure 7 also shows that the smooth surface (plain surface case) shows the highest minimum temperature of the group since it has less available area to dissipate the heat coming from the hot source.

5.2.1. Predictions

Figure 8 shows a representation of the deviation of the predictions from its real value by means of a scatter plot with a reference *xy* line for the desirable result. It has been found that the architecture from random forest is not the most suitable for predicting fin performance. Overall, the point clouds from $\dot{Q}_{\text{FINS}}$, $\bar{T}$ and T_{MIN} show both higher dispersion and higher MAPE results for the predictions.

In particular, the heat flux is especially complicated to model, which is believed to be influenced by the most limiting cases (those close to low to nonexistent heat transfer, acting as deflectors). Considering that such cases only consist of 1% of the total database, it is not possible to have a sufficiently representative sample for the model to be able to generalize to heat conservation and dissipation circumstances under the

Figure 8. Random forest regressor and MLP results for $\dot{Q}_{\mathrm{FINS}}$, $\bar{T}$ and T_{MIN} (from left to right).
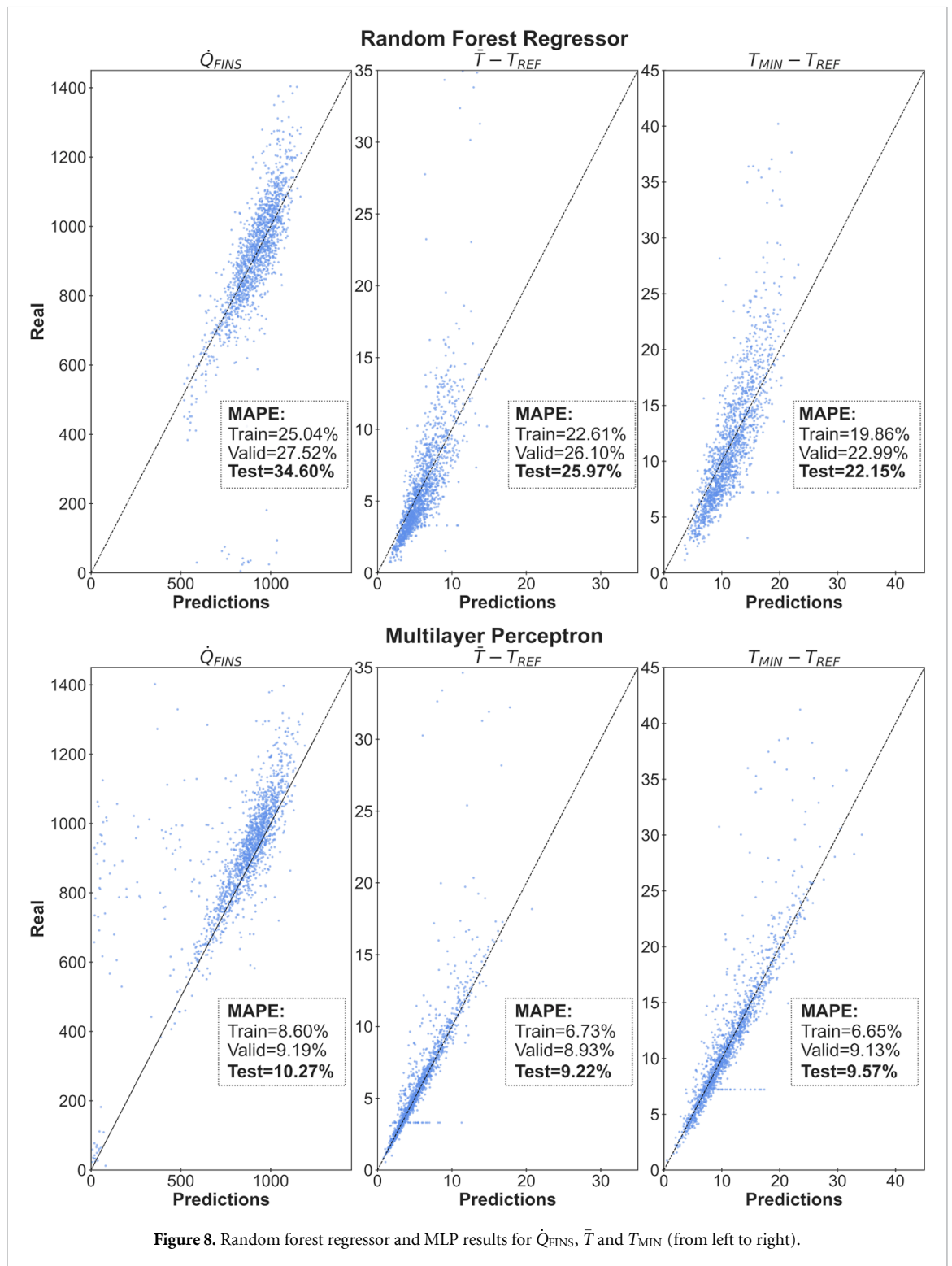
same algorithm architecture. Therefore, it is believed that either a larger sample size or a different model for each purpose could give a better result thereby eliminating unnecessary external noise.

A summary of the metrics obtained during the model tuning for the optimal architecture (detailed in table 5) can be found in table 4.

For the random forest regressor, the number of examples required as minima at each node separation, as well as at each terminal node, had to be set at a value somewhat higher than expected (above 10) at its optimum to avoid overfitting the data during training. This hindered its subsequent generalization.

Table 4. Random forest regressor and MLP error results for $\dot{Q}_{\mathrm{FINS}}$, $\bar{T}$ and T_{MIN}.

	Random forest regressor								
	$\dot{Q}_{\mathrm{FINS}}$			$\bar{T} - T_{\mathrm{REF}}$			$T_{\mathrm{MIN}} - T_{\mathrm{REF}}$		
Metric	Train	Valid	Test	Train	Valid	Test	Train	Valid	Test
MAPE	25.04%	27.52%	34.60%	22.62%	26.1%	25.97%	19.86%	22.99%	22.15%
MSE	1.04×10^4	1.29×10^4	1.27×10^4	6.38	7.96	7.57	9.01	11.60	10.74
	Multilayer perceptron								
	$\dot{Q}_{\mathrm{FINS}}$			$\bar{T} - T_{\mathrm{REF}}$			$T_{\mathrm{MIN}} - T_{\mathrm{REF}}$		
Metric	Train	Valid	Test	Train	Valid	Test	Train	Valid	Test
MAPE	8.60%	9.19%	10.27%	6.73%	8.93%	9.22%	6.65%	9.13%	9.57%
MSE	1.87×10^4	1.88×10^4	2.77×10^4	5.07	5.44	5.76	4.16	4.92	5.58

Table 5. Hyperparameters for the random forest regressor and MLP.

	Random forest regressor			
Hyperparameters		$\dot{Q}_{\mathrm{FINS}}$	$\bar{T} - T_{\mathrm{REF}}$	$T_{\mathrm{MIN}} - T_{\mathrm{REF}}$
1	N° of decision trees.	700	700	700
2	Max. depth of each individual tree.	15	15	15
3	Max. n° of features considered when evaluating a split.	6	6	6
4	Minimum n° of samples needed to split a node.	30	20	20
5	Minimum n° of samples required to be a leaf node.	20	20	20
6	Perform bootstrap.	True	True	True
	Multilayer perceptron			
Hyperparameters		$\dot{Q}_{\mathrm{FINS}}$	$\bar{T} - T_{\mathrm{REF}}$	$T_{\mathrm{MIN}} - T_{\mathrm{REF}}$
1	Batch size.	128	32	64
2	Activation function.	—	RELU	RELU
3	Optimizer.	SGD	adam	rmsprop
4	Neurons.	300	200	200

5.3. Pressure drop

Pressure drop occurs in any flow where there is a variation between the inlet and outlet pressure, being higher at the former. This behavior can both positively and negatively affect the heat transfer process. The negative effect of a large pressure drop implies that higher pump power is needed to push the flow around the circuit, thus leading to higher electricity consumption and greater costs. In addition, in a two-phase flow where either boiling or condensation was experienced, the higher the pressure drop was, the lower the local saturation temperature of the fluid, which directly affected the heat transfer. In contrast, a higher pressure drop can also be indicative of higher turbulence, thus improving heat exchange since the heat transfer in the laminar flow film is negligible due to the absence of convective heat exchange.

The interest behind the designs tested in the present work focuses on taking advantage of the increased turbulence in the area known as the 'viscous layer', where most of the heat transfer resistance is found. Understanding the behavior in such a small domain is vital to finding new geometries that increase the heat exchange in this nearby wall region.

Figure 9 shows the summary of the pressure drop and drag coefficients of the geometries included in the present database. The former follows a normal-like distribution centered at approximately 7 Pa mm^{-1}, and the latter (represented as variable D for total drag in the top right-hand side) shows a truncated normal-like distribution with slightly higher density toward values below 0.27. This is caused by the friction drag contribution (i.e. C_F) that is fully concentrated between 0.05 and 0.10, deviating the normalized distribution that was originally followed by the pressure drag, i.e. C_F.

Figure 9. On the left, histograms of pressure, skin friction and drag coefficients (top), and DP/L (bottom). On the right, a heatmap reflecting the intersection between the drag coefficient and DP/L. Moreover, the plain surface (i.e. baseline) case is plotted for reference in the heatmap.
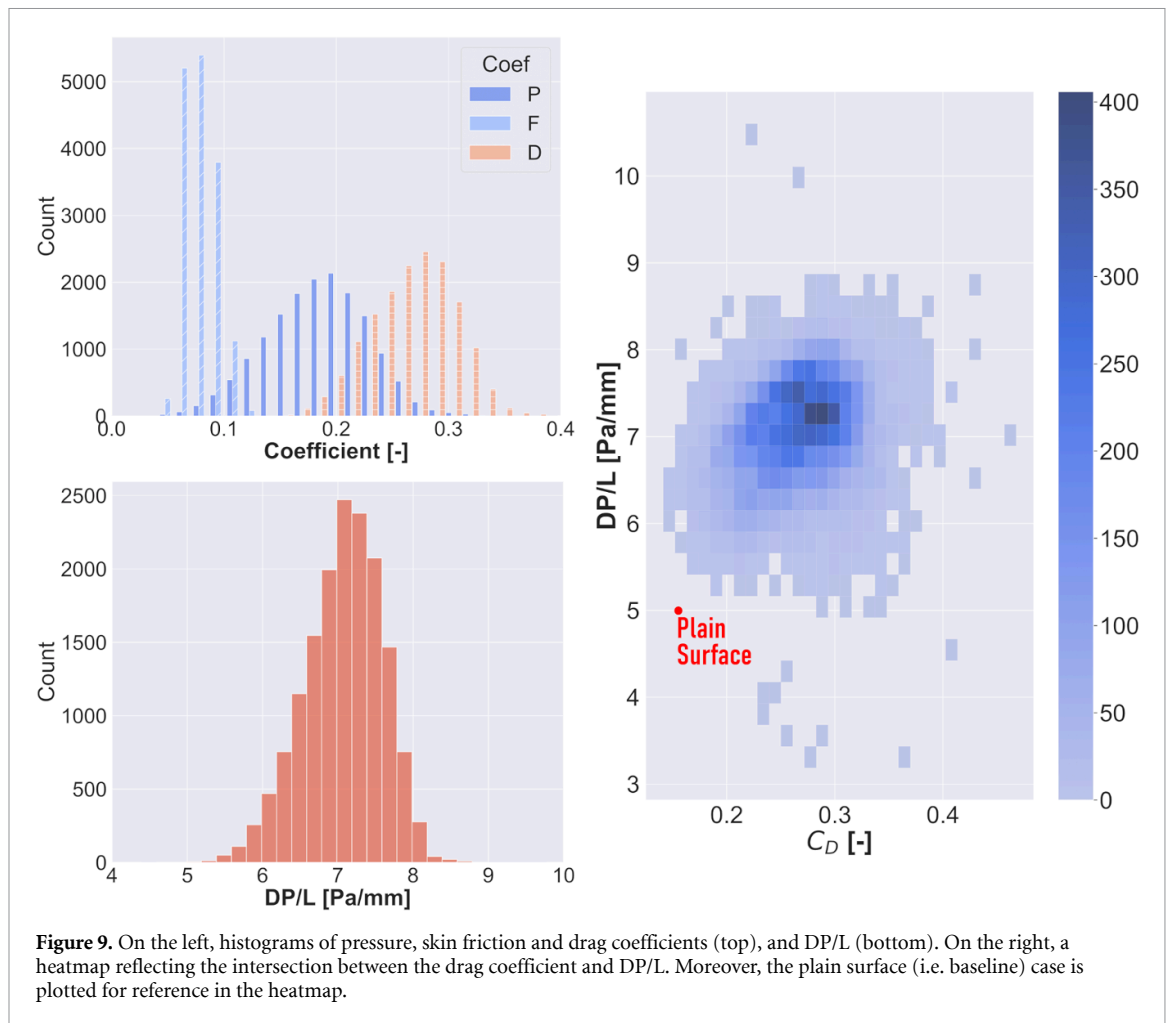
Moreover, in the heatmap included in figure 9, it is interesting to note the relative position of the plain surface case compared to the rest. The smooth surface does not have any obstacle that hampers the fluid flow. Thus, it experiences the lowest pressure drop and subsequent drag. In addition to a few nonrepresentative outliers, the majority of the results are situated above such a reference location, and as expected, geometries that encounter a higher pressure drop tend also to lead to a higher total drag coefficient.

5.3.1. Predictions

The results obtained in the case of fluid dynamic variables are very promising in the case of MLP (figure 10) and deviate to a greater extent from true values for random forest predictions. In the case of the pressure drop, they include a larger dispersion toward the boundaries, being less aligned with the optimal prediction (represented by the dashed line). On the other hand, a similar behavior is experienced in the drag coefficients; although for the total drag the results are closer to the actual values, both the pressure drag coefficient (with a dispersion along the entire region) and the friction drag coefficient (mostly deviated for values greater than 0.10, which do represent a minority of the sample as it is shown in figure 9) are far from the result obtained with the MLP.

By looking at the outcome obtained with a simple network, such as an MLP, the outstanding results are quite remarkable, being especially representative of the total drag with an MAPE of 1.31% in the test set and no detected overfitting. With hardly any outliers in the predictions, these results are promising for the subsequent use of the model in the extrapolation of results for enhanced surfaces not yet evaluated.

Table 6 includes a summary of the metrics obtained during the model tuning, where the prediction of all drag coefficients by the MLP stands out for its outstanding values. Details on the architecture are shown in table 7.

Figure 10. Random forest regressor and MLP results for DP/L, C_D, C_P and C_F (from left to right).
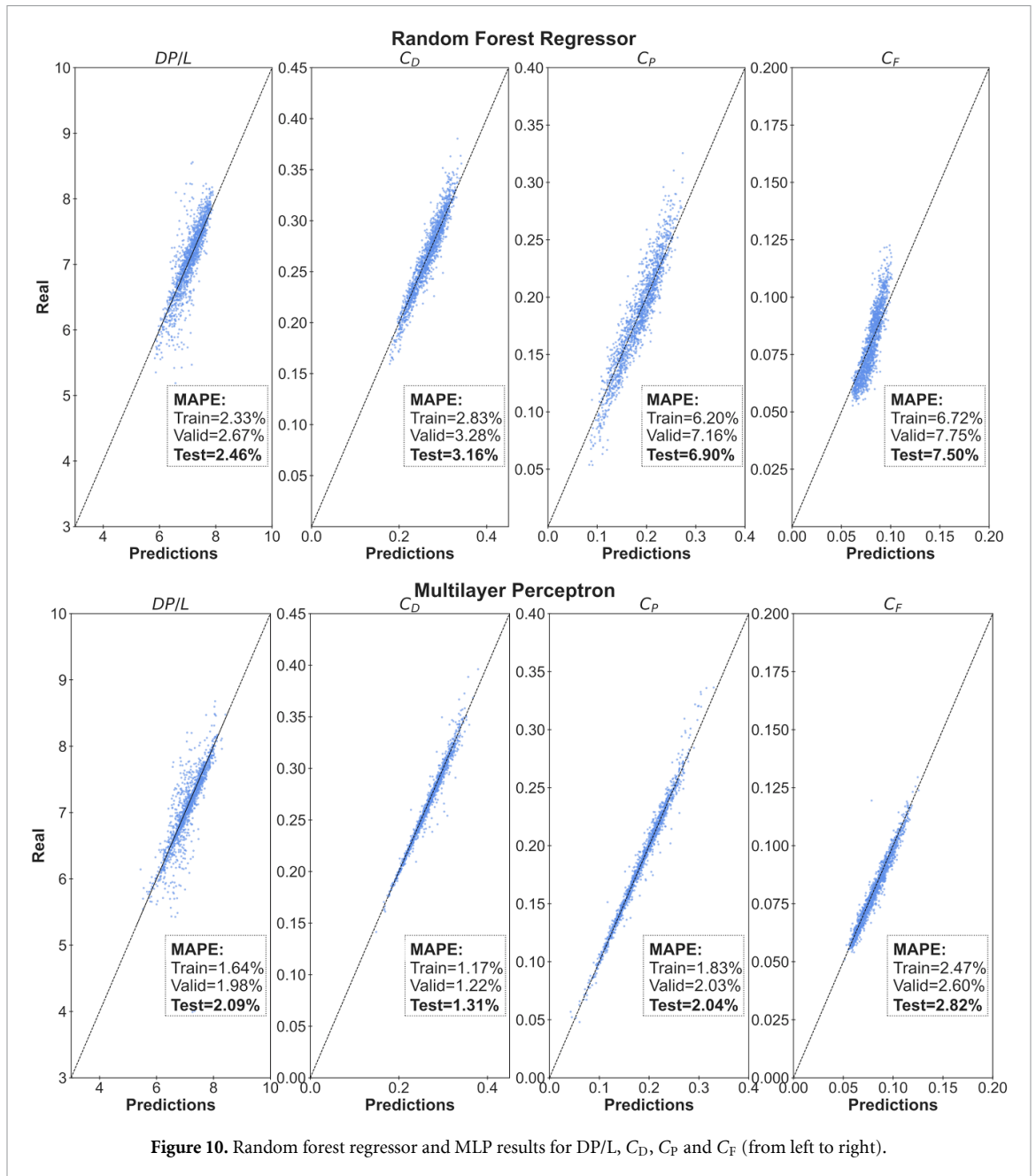
It is interesting to note that given the success of the machine learning techniques employed, the applicability of the methodology could be extended to regions of turbulent flow where nonlinearities play a greater role in the characterization of the data. Even so, as the complexity of the patterns within data increases, one would expect to need to readjust the models' architectures to obtain an accuracy similar to that shown in tables 4 and 6.

Table 6. Random forest regressor and MLP error results for DP/L, C_D, C_P and C_F.

		Random forest regressor				
		DP/L			C_D	
Metric	Train	Valid	Test	Train	Valid	Test
MAPE	2.33%	2.67%	2.45%	2.83%	3.28%	3.16%
MSE	6.35×10^{-2}	8.08×10^{-2}	6.61×10^{-2}	1.05×10^{-4}	1.37×10^{-4}	1.18×10^{-4}
		C_P			C_F	
Metric	Train	Valid	Test	Train	Valid	Test
MAPE	6.20%	7.16%	6.90%	6.72%	7.76%	7.50%
MSE	1.92×10^{-4}	2.52×10^{-4}	2.28×10^{-4}	4.72×10^{-5}	6.17×10^{-5}	5.56×10^{-5}
		Multilayer perceptron				
		DP/L			C_D	
Metric	Train	Valid	Test	Train	Valid	Test
MAPE	1.64%	1.98%	2.09%	1.17%	1.22%	1.31%
MSE	0.046	0.063	0.065	2.75×10^{-5}	3.00×10^{-5}	3.40×10^{-5}
		C_P			C_F	
Metric	Train	Valid	Test	Train	Valid	Test
MAPE	1.83%	2.03%	2.04%	2.47%	2.59%	2.82%
MSE	2.84×10^{-5}	3.32×10^{-5}	3.35×10^{-5}	6.90×10^{-6}	7.67×10^{-6}	9.22×10^{-6}

Table 7. Hyperparameters for the random forest regressor and MLP.

	Random forest regressor				
Hyperparameters		DP/L	C_D	C_P	C_F
1	N° of decision trees.	600	700	700	700
2	Max. depth of each individual tree.	15	15	15	15
3	Max. n° of features considered when evaluating a split.	6	6	6	6
4	Minimum n° of samples needed to split a node.	20	30	20	20
5	Minimum n° of samples required to be a leaf node.	20	20	20	20
6	Perform bootstrap.	True	True	True	True
	Multilayer perceptron				
Hyperparameters		DP/L	C_D	C_P	C_F
1	Batch size.	128	32	32	64
2	Activation function.	—	RELU	—	—
3	Optimizer.	adam	adam	adam	adam
4	Neurons.	100	100	100	200

6. Conclusions

This work has demonstrated the ability of machine learning algorithms to learn surrogate models to predict both the thermal and fluid dynamic behavior of a cooling fin from geometric coordinates. Specifically, we compare random forests and neural networks trained on an extensive CFD database. The MLP neural network models performed well consistently, while the random forest method had too much performance variability.

Among the various outcomes learned from the present work, the importance of a correct sampling of the parametric search space has been observed. While it is true that cases considered to be extreme have been left in the database due to their interest in certain industrial applications, this small set of cases (below 1% of the total sample) seems to have been identified by the model as noise rather than representative data. This affects the accuracy of the results, with the close-to-null heat flux cases being overpredicted when using the random forest algorithm. On the other hand, MLP demonstrates a better ability to adapt to such extreme designs.

The ease of learning by the neural network of fluid dynamic variables (both pressure drop and drag coefficients) from geometric coordinates has been shown, with relative errors under 2.82% on the test results. Although for random forest the learning is not as precise (with relative error over 2% for the pressure drop and total drag, and approximately 7% for the pressure drag and skin friction), it does show a better performance than for the thermal variables (whose relative error was close to 25% for all the predictions).

In general, the MLP is the most successful architecture in characterizing the microenhanced surface. It shows great potential for its use as a surrogate CFD model for future implementation in geometry optimization schemes. Such a study could be focused on either maximizing or minimizing any of the outputs predicted by the models. In this way, the surrogate model could be adapted to a specific application's need.

Data availability statement

The data that support the findings of this study are available from the authors upon reasonable request.

Acknowledgments

Appendix
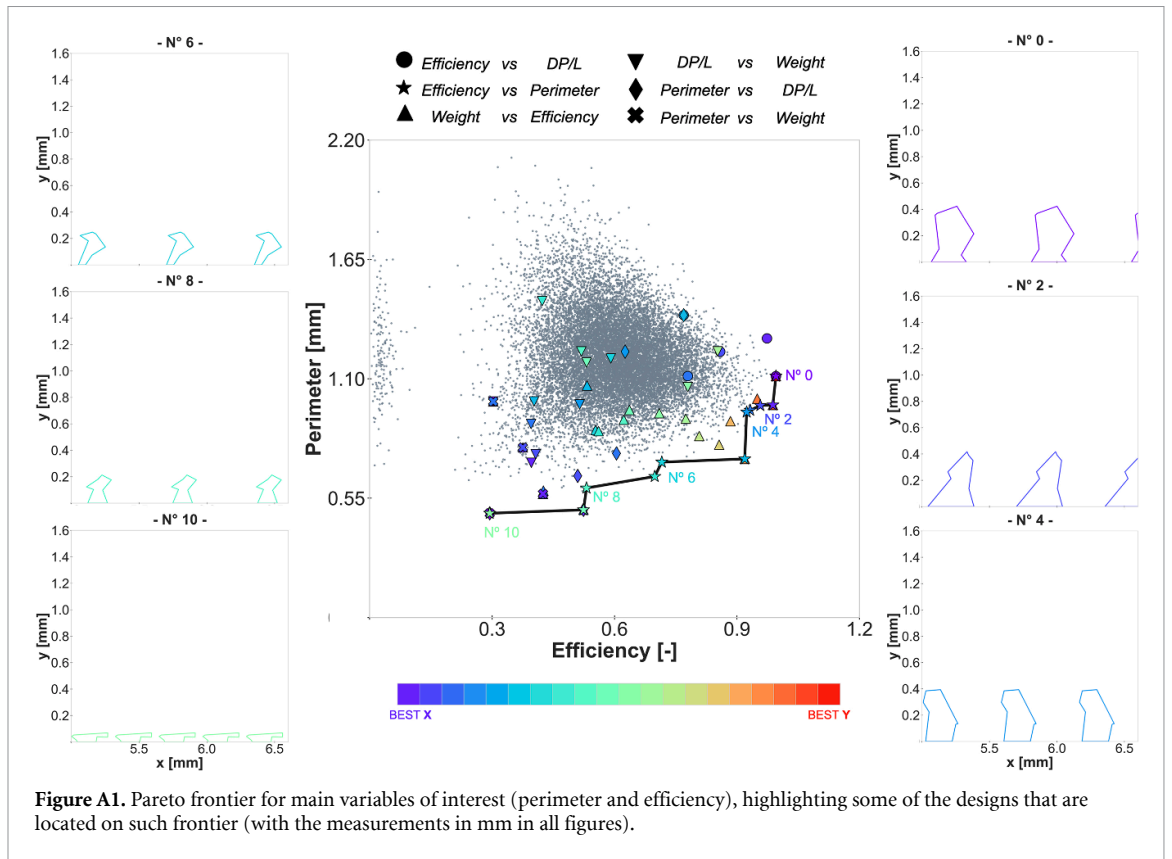
Figure A1. Pareto frontier for main variables of interest (perimeter and efficiency), highlighting some of the designs that are located on such frontier (with the measurements in mm in all figures).
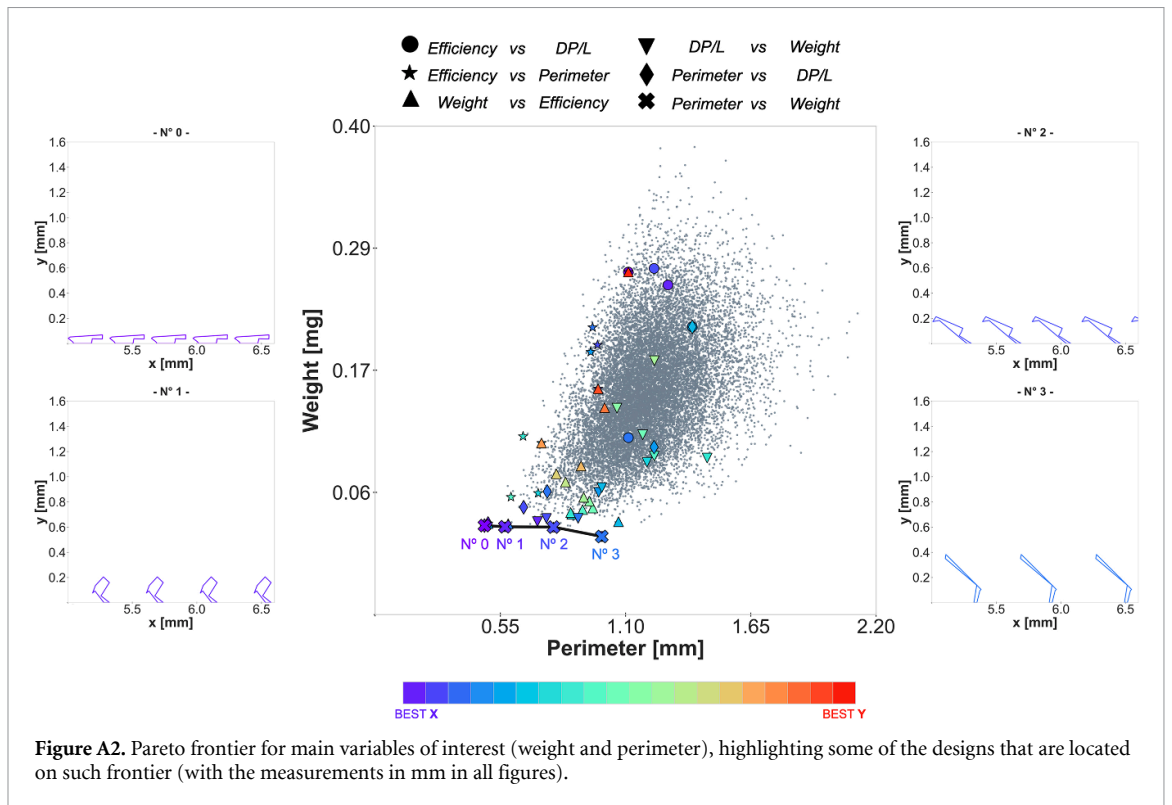
Figure A2. Pareto frontier for main variables of interest (weight and perimeter), highlighting some of the designs that are located on such frontier (with the measurements in mm in all figures).

ORCID iD

J Porteiro ⬤ https://orcid.org/0000-0003-2197-3269

References

[1] Cárdenas B and León N 2013 High temperature latent heat thermal energy storage: phase change materials, design considerations and performance enhancement techniques *Renew. Sustain. Energy Rev.* **27** 724–37

[2] Buidin T I C and Mariasiu F 2021 Battery thermal management systems: current status and design approach of cooling technologies *Energies* **14** 4879

[3] Song Y, Gong S, Vaartstra G and Wang E N 2021 Microtube surfaces for the simultaneous enhancement of efficiency and critical heat flux during pool boiling *ACS Appl. Mater. Interfaces* **13** 12629–35

[4] Manglik R M and Bergles A E 2004 Enhanced heat and mass transfer in the new millennium: a review of the 2001 literature *J. Enhanc. Heat Transf.* **11** 87–118

[5] McDonough J R 2020 A perspective on the current and future roles of additive manufacturing in process engineering, with an emphasis on heat transfer *Therm. Sci. Eng. Prog.* **19** 100594

[6] Knight R W, Goodling J S, Hall D J and Jaeger R C 1992 Heat sink optimization with application to microchannels *IEEE Trans. Compon. Hybrids Manuf. Technol.* **15** 832–42

[7] Ghorbani N, Targhi M Z, Heyhat M M and Alihosseini Y 2022 Investigation of wavy microchannel ability on electronic devices cooling with the case study of choosing the most efficient microchannel pattern *Sci. Rep.* **12** 5882

[8] Slomski E M, Fischer S, Scheerer H, Oechsner M and Stephan P 2013 Textured CrN thin coatings enhancing heat transfer in nucleate boiling processes *Surf. Coat. Technol.* **215** 465–71

[9] Liu H, Li B, Zhang L and Li X 2020 Optimizing heat-absorption efficiency of phase change materials by mimicking leaf vein morphology *Appl. Energy* **269** 114982

[10] Li B, Hong J, Yan S, Liu H and Ge L 2017 Generating optimal heat conduction paths based on bionic growth simulation *Int. Commun. Heat Mass Transfer* **83** 55–63

[11] Goh A L and Ooi K T 2016 Nature-inspired inverted fish scale microscale passages for enhanced heat transfer *Int. J. Therm. Sci.* **106** 18–31

[12] Oyama A, Nonomura T and Fujii K 2010 Data mining of pareto-optimal transonic airfoil shapes using proper orthogonal decomposition *J. Aircr.* **47** 1756–62

[13] Cavazzuti M and Corticelli M A 2008 Optimization of heat exchanger enhanced surfaces through multiobjective genetic algorithms *Numer. Heat Transfer* A **54** 603–24

[14] Karkaba H, Dbouk T, Habchi C, Russeil S, Lemenand T and Bougeard D 2020 Multi objective optimization of vortex generators for heat transfer enhancement using large design space exploration *Chem. Eng. Process.* **154** 107982

[15] Andrés E, Salcedo-Sanz S, Monge F and Pérez-Bellido A M 2012 Efficient aerodynamic design through evolutionary programming and support vector regression algorithms *Expert Syst. Appl.* **39** 10700–8

[16] Fukagata K, Kern S, Chatelain P, Koumoutsakos P and Kasagi N 2008 Evolutionary optimization of an anisotropic compliant surface for turbulent friction drag reduction *J. Turbulence* **9** N35

[17] Gazzola M, Vasilyev O V and Koumoutsakos P 2011 Shape optimization for drag reduction in linked bodies using evolution strategies *Comput. Struct.* **89** 1224–31

[18] See Y S, Ho J Y, Leong K C and Wong T N 2022 Experimental investigation of a topology-optimized phase change heat sink optimized for natural convection *Appl. Energy* **314** 118984

[19] Može M, Zupančič M and Golobič I 2020 Pattern geometry optimization on superbiphilic aluminum surfaces for enhanced pool boiling heat transfer *Int. J. Heat Mass Transfer* **161** 120265

[20] Singh M, Datla N V, Kondaraju S and Bahga S S 2018 Enhanced thermal performance of micro heat pipes through optimization of wettability gradient *Appl. Therm. Eng.* **143** 350–7

[21] Cora Ö N, Usta Y H and Koç M 2009 Micro-manufacturing of micro-scale porous surface structures for enhanced heat transfer applications: an experimental process optimization study *J. Micromech. Microeng.* **19** 045011

[22] Moon M-A, Husain A and Kim K-Y 2012 Multi-objective optimization of a rotating cooling channel with staggered pin-fins for heat transfer augmentation *Int. J. Numer. Methods Fluids* **68** 922–38

[23] Zhou F, Hansen N and Catton I 2010 Obtaining closure for heat exchanger modeling based on volume averaging theory (VAT) 14th *Int. Heat Transfer Conf.* (*Washington, DC, USA, 8–13 August*) pp 693–701

[24] Zhou J, Hatami M, Song D and Jing D 2016 Design of microchannel heat sink with wavy channel and its time-efficient optimization with combined RSM and FVM methods *Int. J. Heat Mass Transfer* **103** 715–24

[25] Maradiya C, Vadher J and Agarwal R 2018 The heat transfer enhancement techniques and their thermal performance factor *Beni-Suef Univ. J. Basic Appl. Sci.* **7** 1–21

[26] Iyer J, Moore T, Nguyen D, Roy P and Stolaroff J 2022 Heat transfer and pressure drop characteristics of heat exchangers based on triply periodic minimal and periodic nodal surfaces *Appl. Therm. Eng.* **209** 118192

[27] Jambunathan K, Hartle S L, Ashforth-Frost S and Fontama V N 1996 Evaluating convective heat transfer coefficients using neural networks *Int. J. Heat Mass Transfer* **39** 2329–32

[28] Ashforth-Frost S, Fontama V N, Jambunathan K and Hartle S L 1995 The role of neural networks in fluid mechanics and heat transfer 1995 *IEEE Instrumentation and Measurement Technology Conf.* (*Waltham, MA, USA*) p 6

[29] Vinuesa R, Azizpour H, Leite I, Balaam M, Dignum V, Domisch S, Felländer A, Langhans S D, Tegmark M and Fuso Nerini F 2020 The role of artificial intelligence in achieving the sustainable development goals *Nat. Commun.* **11** 233

[30] Kapteyn M G and Willcox K E 2020 From physics-based models to predictive digital twins via interpretable machine learning (arXiv:200411356)

[31] Fan D, Jodin G, Consi T R, Bonfiglio L, Ma Y, Keyes L R, Karniadakis G E and Triantafyllou M S 2019 A robotic intelligent towing tank for learning complex fluid-structure dynamics *Sci. Robot.* **4** eaay5063

[32] Niederer S A, Sacks M S, Girolami M and Willcox K 2021 Scaling digital twins from the artisanal to the industrial *Nat. Comput. Sci.* **1** 313–20

[33] Brenner M P, Eldredge J D and Freund J B 2019 Perspective on machine learning for advancing fluid mechanics *Phys. Rev. Fluids* **4** 100501

[34] Duraisamy K, Iaccarino G and Xiao H 2019 Turbulence modeling in the age of data *Annu. Rev. Fluid Mech.* **51** 357–77

[35] Kasagi N, Hasegawa Y, Fukagata K and Iwamoto K 2012 Control of turbulent transport: less friction and more heat transfer *J. Heat Transfer* **134** 031009

[36] Vinuesa R and Brunton S L 2022 Enhancing computational fluid dynamics with machine learning *Nat. Comput. Sci.* **2** 358–66

[37] Dupuis R, Jouhaud J-C and Sagaut P 2018 Surrogate modeling of aerodynamic simulations for multiple operating conditions using machine learning *AIAA J.* **56** 3622–35

[38] Brunton S L, Noack B R and Koumoutsakos P 2020 Machine learning for fluid mechanics *Annu. Rev. Fluid Mech.* **52** 477–508

[39] Breiman L 2001 Random forests *Mach. Learn.* **45** 5–32

[40] Géron A 2019 *Hands-On Machine Learning with Scikit-Learn, Keras, and TensorFlow: Concepts, Tools, and Techniques to Build Intelligent Systems* (Sebastopol, CA: O'Reilly Media, Inc.)

[41] Geurts P, Ernst D and Wehenkel L 2006 Extremely randomized trees *Mach. Learn.* **63** 3–42

[42] Goodfellow I, Bengio Y and Courville A 2016 *Deep Learning* (Cambridge, MA: The MIT Press)

[43] Refaeilzadeh P, Tang L and Liu H 2009 Cross-Validation *Encyclopedia of Database Systems* ed L Liu and M T Özsu (Boston, MA: Springer) pp 532–8

[44] Webb R L and Kim N H 2005 *Principles of Enhanced Heat Transfer* (Boca Raton: Taylor & Francis) (https://doi.org/10.1201/b12413)